Giner-Sanz, JJ.; Ortega Navarro, EM.; Pérez-Herranz, V. (2018). Statistical analysis of the effect of temperature and inlet humidities on the parameters of a semiempirical model of the internal resistance of a polymer electrolyte membrane fuel cell. Journal of Power Sources. 381:84-93. https://doi.org/10.1016/j.jpowsour.2018.01.093

Statistical analysis of the effect of temperature and inlet humidities on the parameters of a semiempirical model of the internal resistance of a Polymer Electrolyte Membrane Fuel Cell

J. J. Giner-Sanz, E. M. Ortega, V. Pérez-Herranz*

IEC group, Depto. Ingeniería Química y Nuclear, Universitat Politècnica de València

Camino de Vera S/N, 46022 Valencia, Spain

*Corresponding author. Tel.: +34-96-3877632; fax: +34-96-3877639;

E-mail address: vperez@iqn.upv.es (V. Pérez-Herranz)

Abstract

The internal resistance of a PEM fuel cell depends on the operation conditions and on the current delivered by the cell. This work's goal is to obtain a semiempirical model able to reproduce the effect of the operation current on the internal resistance of an individual cell of a commercial PEM fuel cell stack; and to perform a statistical analysis in order to study the effect of the operation temperature and the inlet humidities on the parameters of the model. First, the internal resistance of the individual fuel cell operating in different operation conditions was experimentally measured for different DC currents, using the high frequency intercept of the impedance spectra. Then, a semiempirical model based on Springer and co-workers' model was proposed. This model is able to successfully reproduce the experimental trends. Subsequently, the curves of resistance versus DC current obtained for different operation conditions were fitted to the semiempirical model, and an analysis of variance (ANOVA) was performed

in order to determine which factors have a statistically significant effect on each model parameter. Finally, a response surface method was applied in order to obtain a regression model.

Keywords: Electrochemical Impedance Spectroscopy, Internal Resistance, Membrane Water Content, PEM Fuel Cell, Statistical Analysis.

1. Introduction

The need of a clean, efficient and reliable energy vector has led to the development of fuel cell technology [1]. Fuel cells (FCs) are electrochemical devices that transform the chemical energy contained in a fuel, directly into electricity. PEM fuel cells (PEMFCs) are a particular type of FC in which a proton exchange membrane (PEM) is used as electrolyte. In recent years, this type of FC has been considered a very promising alternative for power generation devices for automotive, portable and distributed applications [2]. The main advantages of PEMFCs are their compactness [3], their high power density [4], their light weight and low cost [5], their low environmental load [6, 7], and their high efficiency [8, 9]. However, there are still issues that have to be tackled in order to make them economically competitive. For this reason, great research efforts have been made in recent years in order to increase the performance [10-13] and the reliability [14-19] of such FCs, and to decrease their cost [20-23].

The internal resistance is a key parameter to characterize the performance of a PEMFC [24], since it determines the ohmic losses within the PEMFC. According to Ohm's law:

$$\eta_{Ohmic} = I \cdot R_{int} \qquad (1)$$

Where η_{Ohmic} denotes the ohmic overvoltage; I stands for the current delivered by the PEMFC; and R_{int} corresponds with the internal resistance of the PEMFC. This parameter encompasses 3 major contributions: the electronic resistance (R_{int}^{ele}), the ionic resistance (R_{int}^{ion}), and the contact resistance (R_{cont}). On the one hand, R_{int}^{ele} arises from the

resistance to the electron flow in the electronic conductors of the PEMFC (e.g. graphite electrodes and current collectors). On the other hand, R_{int}^{ion} arises from the resistance to protonic flow in the ionic conductors of the PEMFC (e.g. PEM membrane). Finally, R_{cont} corresponds with the contact resistance between the different conductors of the PEMFC. The internal resistance of a PEMFC depends mainly on the operation conditions and on the polarization current at which the fuel cell is operated [25].

A large variety of PEM resistance models can be found in literature [26]. These models can be classified in two main types: microscopic and macroscopic models. On the one hand, microscopic models [27-34] try to explain the trends in PEM resistance starting from the ion/solvent/polymer interactions in the molecular level (v.g. Grotthus mechanism). On the other hand, macroscopic models relate PEM resistance to macroscopic variables, such as the water content of the membrane, the current delivered by the PEMFC or the temperature. In this type of PEMFC internal resistance models, several groups can be identified. The simplest one is the constant resistance model [35], in which the resistance of the membrane is considered as a constant. Some authors [36] modify the constant resistance model considering an Arrhenius-like-expression for modelling the effect of the temperature on the PEMFC internal resistance. Another group of macroscopic internal resistance models [37-41] is formed by the models that are based on the empirical model proposed by Amphlett and co-workers [42]. This model consists in a quadratic regression model with two independent factors: temperature and delivered current. In many cases, the quadratic (T^2 and I^2) and the interaction ($T \cdot I$) terms are neglected [39]. This assumption reduces the model to a simple linear regression model [43]. The parameters of the empirical model can only

be obtained by fitting the model to experimental data. Other macroscopic internal resistance models that have extensively been used in literature are the diffusive flow type models [44-46], and the hydraulic flow type models [47-49]. The diffusion models are based on the empirical expression proposed by Springer and co-workers [44], or on one of its variants. These empirical expressions relate the membrane resistivity with its water content. Some works [50] consider the water content parameter as an adjustable parameter; while others [51-53] calculate it using the expression relating the water content parameter with the water vapour activity, presented in [54]. Meanwhile, the hydraulic models are based on the model developed by Bernardi and Verbrugge [47]. Apart from these main types of macroscopic models, other less common models can be found in literature, such as models that use the chemical potential as the driving force [55-57], or two-phase models [58] that include the simultaneous presence of liquid water and vapour in the PEM.

The goal of this work is to obtain a semiempirical model able to simulate the effect of the operation current on the internal resistance of a single cell of a 300 W commercial PEMFC stack; and to study the effect of the operation conditions (temperature and inlet humidities) on the parameters of the proposed semiempirical model. The present study is based on the diffusive flow type model developed by Springer et al. [44]. This work's objective is to build a simple semiempirical model able to predict the internal resistance of a PEMFC, and to validate it using experimental data. In order to fulfil this goal, the internal resistance of a single cell of a commercial PEMFC stack was measured experimentally by electrochemical impedance spectroscopy (EIS) at different operation currents, and at different operation conditions (temperature and inlet humidities). A

semiempirical model was proposed in order to reproduce the effect of the operation current on the internal resistance. The proposed semiempirical model was fit to the R_{int} vs I experimental curves obtained for different operation conditions. In this way, the value of the model parameters was obtained for different temperatures and inlet humidities. Finally, a statistical analysis was performed on the obtained results, in order to determine the effect of the operation conditions on the parameters of the semiempirical model. Firstly, an analysis of variance (ANOVA) analysis was performed in order to determine which operation conditions have a statistically significant effect on each model parameter. Then, a surface response method was applied in order to obtain a black box model relating each model parameter to the operation factors that have a significant effect on it.

2. Experimental design

A full 2^3 replicated factorial design with centerpoint was used in this work. This kind of experimental design consists in an experimental design where 3 factors are studied at 2 levels: level -1 and level +1. On the one hand, full factorial designs involve running in each replicate, all the 2^3 combinations of 3 factors at 2 levels. On the other hand, replication consists in the repetition of the whole set of treatments defined in the factorial design. Finally, a centerpoint consists in a treatment in which all factors are at level 0, defined as the arithmetic mean of levels -1 and +1. One of the main reasons for including centerpoints in an experimental design is that they allow to identify curvatures in the output variables. This experimental design is much more efficient than the traditional sequential experimental design, since it requires fewer experiments to analyse a given number of input factors, and it allows to study the interaction between the considered factors [59].

The three factors that were considered in this work were the operation temperature, the humidity of the hydrogen inlet, and the humidity of the air inlet. Table 1 sums up the 3 levels considered for each one of these factors. On the one side, the temperature levels were selected according to the nominal temperature operation range of the commercial PEMFC. On the other side, as it will be explained in section 3, the experimental setup allows to control the humidification temperatures, and not directly the inlet gas humidities. Preliminary experimentation was performed in order to obtain the relation between the gas humidity and the humidification temperature. Level +1 of the humidity factors were selected considering a humidification temperature of $70℃$,

the maximum humidification temperature allowed by the humidification system. While level -1 of the humidity factors were selected considering a humidification temperature of 30℃. In this work, all the humidities are expressed as absolute humidities, in units of $g_{H_2O} \cdot g_{dry\ gas}^{-1}$.

In this work, experiments were identified with a sign triplet, in which each sign denotes the level of the corresponding experimental factor. For instance, experiment (-;-;+) denotes the experiment in which the operation temperature is in level -1 (30℃), the hydrogen humidification temperature is in level -1 (30℃), and the air humidification temperature is in level +1 (70℃).

3. Methodology and experimental procedure

First, for each one of the 18 treatments (set of operation conditions) considered in this work's experimental design, the internal resistance of an individual cell of a commercial PEMFC stack was experimentally measured for different operation currents. In order to achieve this, the electrochemical impedance spectrum of the individual cell was measured at different polarization currents, for each one of the experiments considered in the experimental design. The EIS measurements were done using the experimental setup shown in Figure 3 of reference [60].

The main element of the experimental setup is a 300W commercial PEMFC stack, provided by HeliocentriS®, composed by 20 individual cells, with an effective area of 58 cm^2. The MEA consists of a Nafion® 117 membrane with a total platinum loading of 0.4 $mg \cdot cm^{-2}$. The diffusion layers are made out of graphite. The air supply is provided by a compressor and the hydrogen comes from a 200 bar high-pressure storage tank. The humidification of the gas inlets is assured by a humidification system and the fuel cell stack operating temperature is controlled by a refrigeration system. On the one hand, the humidification system consists in two independent bubbling humidification systems, with humidification temperature control. On the other hand, the refrigeration system consists in a heat exchanger equipped with a continuous pump and a temperature controller. The reactant gases flow rates are controlled using mass flow controllers. The reactant inlet pressures are monitored by pressure gauges and are regulated using manual valves. All the relevant system temperatures are monitored by thermocouples. The overall control was done using a control computer with a Labview® application. All

the experiments were carried out in open end anode mode, with constant inlet reactant flow rates: $5\ NL \cdot min^{-1}$ for the hydrogen stream and $35\ NL \cdot min^{-1}$ for the air stream.

The individual cell galvanostatic impedance spectra were obtained using an Autolab® 302N potentiostat/galvanostat with FRA module and 20 A booster, controlled using NOVA® software. The selected frequency range extended from 5 kHz to 10 mHz, with 50 frequencies logarithmically spaced. Table 2 lists the measurement parameters used in this work to perform the EIS measurements. These measurement parameters were selected in a previous work [61]. All the EIS measurements were done using the optimum perturbation amplitude determined in a recent work [60].

For each experiment (set of operation conditions), the EIS spectra were measured at different operation currents: 0.5A, 1A, 2A, …, up to a maximum operation current that guarantees that no polarity inversion occurs in any point of the EIS measurement cycle. EIS measurements were obtained in triplicate in order to control the reproducibility of the obtained results. The measurements were not performed sequentially; instead, the order of the measurements was randomized. The randomization strategy allows to orthogonalize the DC current factor and the time factor. In this way, any time drift can be identified. On the contrary, if an increasing amplitude strategy had been selected, it would not be possible to know if the observed trends were due to a time drift of the system, or to the effect of the polarization current.

The preconditioning of the PEMFC system can heavily influence the experimental results, since the preconditioning operation point establishes the water content of the

membrane, and thus determines the membrane resistance [25]. In this work, a preconditioning was done in order to guarantee that the system reaches steady state operation. The preconditioning consisted in operating the PEMFC system at $1.0A$ for 10 minutes in the conditions of the experiment that was going to be performed, before starting the EIS measurements. Moreover, between EIS measurements, the PEMFC system was operated during 10 min at the operation current at which the EIS spectra was going to be measured.

An EIS spectrum is only valid if 3 conditions are achieved: causality, linearity and stability [62]. If any of these conditions is not fulfilled, the obtained spectrum may be misleading and the conclusions extracted from it may be biased or even erroneous [63]. This makes validation a fundamental part of experimental EIS spectra preliminary analysis. In this work, all the experimental EIS spectra were double-validated: they were validated using the linearity assessment method described in previous works [64-66], and the quantitative validation technique based on Kramers-Kronig relations presented in previous works [67-68].

The internal resistance corresponds with the high frequency intersect of the EIS spectrum with the horizontal axis [69]; thus, the internal resistance of the cell for each operation current was determined from the high frequency intersect with the real axis of the experimentally measured impedance spectrum for that operation current. Using this procedure, the R_{int} vs I curve was obtained for each experiment (set of operation conditions). These curves were fitted to the proposed semiempirical model using a nonlinear regression method (Levenberg-Marquardt fitting algorithm). Applying this

methodology, the values of the model parameters were obtained for each one of the 18 experiments.

Finally, an ANOVA statistical analysis was carried out in order to determine which experimental factors have a statistically significant effect on each model parameter. A black box model was built using the response surface method, in order to relate each model parameter with the operation conditions that have a significant effect on it.

4. Experimental results analysis and discussion

4.1. Internal resistance experimental results

Figure 1 shows the detail of the high frequency intercept of the experimental EIS spectra with the real axis, for experiment $(-;-;+)$ (operation temperature: $30℃$; hydrogen humidification temperature: $30℃$; air humidification temperature: $70℃$). A clear trend can be observed in the high frequency intercept with the real axis: it shifts to lower values when the polarization current increases. As stated previously, the high frequency intercept with the real axis gives the value of R_{int}. Using this fact, Figure 2a was obtained from Figure 1. Figure 2a shows the evolution of the internal resistance with the DC current, in experiment $(-;-;+)$. The error bars presented on the graph correspond with the uncertainty (for a 95% confidence level) in the resistance values. This uncertainty arises from the interpolation algorithm that was used to determine the high frequency intercept with the real axis. It can be observed that the internal resistance of the individual cell decreases when I_{DC} increases. The R_{int} vs I_{DC} curve exhibits an asymptotic behaviour: the decline of R_{int} with I_{DC} becomes less pronounced as the operation current increases.

For the sake of clarity, in this work only the experimental results of experiment $(-;-;+)$ were presented. The experimental results obtained in the other 17 experiments were completely analogous to the ones presented here.

The internal resistance values obtained in this work are in agreement with the values presented in literature for similar systems. On the one hand, Ceraolo, Miulli and Pozio [35] measured resistance values in the range $4.0\ m\Omega - 7.0\ m\Omega$. On the other hand, the resistance model proposed by Amphlett and co-workers [43] predicts an internal resistance between $5.0\ m\Omega$ and $10.0\ m\Omega$ in the conditions considered in this work. And finally, Vasiley and co-workers [53] used a value of $3.8\ m\Omega$ for their simulations.

4.2. Semiempirical model

As explained in section 1, the internal resistance of a PEMFC can be broken down into 3 major contributions:

$$\mathrm{R_{int}} = R_{int}^{ele} + R_{int}^{ion} + R_{cont} \qquad (2)$$

In the general case, the ionic resistance of the PEM membrane, $\mathrm{R_{PEM}}$, is several orders of magnitude higher than the other two ohmic contributions [70]; therefore, the following approximation was considered in this work:

$$\mathrm{R_{int}} \approx R_{int}^{ion} = \mathrm{R_{PEM}} \qquad (3)$$

The resistance of the PEM membrane is given by the following expression:

$$\mathrm{R_{PEM}} = \frac{\mathrm{r_{PEM}} \cdot \mathrm{l_{PEM}}}{\mathrm{A_{PEM}}} \qquad (4)$$

Where $\mathrm{A_{PEM}}$ denotes the membrane active area; $\mathrm{l_{PEM}}$ stands for the thickness of the membrane; and $\mathrm{r_{PEM}}$ is the resistivity of the PEM membrane to the proton flow. This parameter depends on the type and characteristics of the PEM membrane, on the temperature and on the level of hydration of the membrane (water content of the membrane) [71]. The PEMFC studied in this work contains a Nafion® 117 membrane. Springer and co-workers developed an experimental model for Nafion® 117 resistivity as a function of temperature and water content [44]:

$$\mathrm{r_{PEM}} = \frac{181.6}{\left(\lambda_{\mathrm{H_2O/SO_3^-}} - 0.634\right) \cdot \mathrm{e}^{4.18 \cdot \left(\frac{\mathrm{T}-303.15}{\mathrm{T}}\right)}} \qquad (5)$$

Where T denotes the operation temperature in K; and $\lambda_{\mathrm{H_2O/SO_3^-}}$ stands for the effective water content of the membrane. This parameter quantifies the effective humidification level of the PEM membrane. Its physical meaning corresponds with the mean number of water molecules per $\mathrm{SO_3^-}$ group. In Nafion® membranes, $\lambda_{\mathrm{H_2O/SO_3^-}} \in]0.634; 22]$. For water contents below the minimum water content ($\lambda_{\min} = 0.634$), the Nafion® membrane becomes a protonic insulator (infinite $\mathrm{r_{PEM}}$). Replacing equations (4) and (5) in (3), the following expression is obtained:

$$R_{int} = \frac{181.6}{\left(\lambda_{H_2O/SO_3^-} - 0.634\right) \cdot e^{4.18 \cdot \left(\frac{T-303.15}{T}\right)}} \cdot \frac{l_{PEM}}{A_{PEM}} \qquad (6)$$

Equation (6) expresses the internal resistance of the PEMFC as a function of known geometrical properties of the membrane (area and thickness), operation temperature and the mean effective water content of the membrane. The following expression for the water content parameter can be obtained from equation (6):

$$\lambda_{H_2O/SO_3^-} = 0.634 + \frac{181.6}{R_{int} \cdot e^{4.18 \cdot \left(\frac{T-303.15}{T}\right)}} \cdot \frac{l_{PEM}}{A_{PEM}} \qquad (7)$$

In the above expression, the water content parameter is expressed as a function of the geometrical characteristics of the PEM membrane, the operation temperature, and the internal resistance of the PEMFC. On the one hand, the geometric constants are known: $A_{PEM} = 58\ cm^2$ and $l_{PEM} = 183\ \mu m$. On the other hand, the operation parameter is one of the factors considered in the experimental design, and therefore, it is known for each experiment. Consequently, expression (7) can be used to estimate parameter λ_{H_2O/SO_3^-} from the experimentally measured internal resistance.

Using the internal resistance experimentally measured (Figure 2a), and equation (7), the water content parameter, λ_{H_2O/SO_3^-}, was calculated for each DC current. The obtained results for experiment $(-; -; +)$ are shown in Figure 2b. It can be observed that initially, the effective water content parameter of the PEM membrane increases with I_{DC}, and then tends asymptotically to a saturation value. The increase of λ_{H_2O/SO_3^-} with the

operation current is due to the production of water on the cathodic compartment as a result of the oxygen reduction half-reaction: by Faraday's law of electrolysis, at higher operation currents, the water production is higher. The increase in water production shifts the water balance of the PEM membrane towards higher water contents. Moreover, a saturation process is observed in the water content curve: a given increase in the DC current causes a larger increase in the water content parameter for low DC currents in comparison to high DC currents. The water content parameter reaches a saturation value: further increases in the DC current do not increase the water content anymore. This is due to the saturation of the membrane: after a certain amount of produced water (fixed by the DC current), the membrane does not take more water; and therefore, the water content of the membrane does not increase further.

Based on the shape of the $\lambda_{\mathrm{H_2O/SO_3^-}}$ versus I_{DC} experimental curve, the following model was proposed in order to capture the evolution of the water content as a function of the operation current:

$$\lambda_{\mathrm{H_2O/SO_3^-}}(I_{DC}) = \lambda^0_{H_2O/SO_3^-} + \left(\lambda^\infty_{H_2O/SO_3^-} - \lambda^0_{H_2O/SO_3^-}\right) \cdot \left(1 - \mathrm{e}^{-\kappa_\lambda \cdot I_{DC}}\right) \quad (8)$$

Taking limits, the following expressions are obtained:

$$\lim_{I_{DC}\to 0} \lambda_{\mathrm{H_2O/SO_3^-}}(I_{DC}) = \lambda^0_{H_2O/SO_3^-} \quad (9)$$

$$\lim_{I_{DC}\to +\infty} \lambda_{\mathrm{H_2O/SO_3^-}}(I_{DC}) = \lambda^\infty_{H_2O/SO_3^-} \quad (10)$$

It can be deduced that $\lambda^{0}_{H_2O/SO_3^-}$ corresponds with the open circuit water content of the membrane (when no current is flowing); $\lambda^{\infty}_{H_2O/SO_3^-}$ is the saturation water content of the membrane; and κ_λ corresponds with the current effect parameter, which quantifies the magnitude of the effect of the operation current on the water content of the membrane. Higher values of κ_λ imply more vertical $\lambda_{\mathrm{H_2O/SO_3^-}}$ versus I_{DC} curves.

Expression (8) was fitted to the experimental data shown in Figure 2b. The obtained fitted model is shown in Figure 2b, superimposed on the experimental data. It can be seen that the proposed empirical model successfully fits the experimental data. Table 3 contains the fitted values of the parameter models, and the determination coefficient. On the one hand, the determination coefficient, 98.57%, shows that the proposed model is able to accurately reproduce the experimental evolution of $\lambda_{\mathrm{H_2O/SO_3^-}}$ with the operation current. On the other hand, the fitted values are consistent with the physical meaning of the model parameters: both, $\lambda^{0}_{H_2O/SO_3^-}$ and $\lambda^{\infty}_{H_2O/SO_3^-}$, are contained in the theoretical $]0.634; 22]$ range.

The literature indicates that a value of $\lambda_{\mathrm{H_2O/SO_3^-}}$ around 22 corresponds with a membrane immersed in water, while a fully hydrated membrane in a PEMFC fed with water-saturated air has a mean value of $\lambda_{\mathrm{H_2O/SO_3^-}}$ around 14 [72]. These values are consistent with the results obtained in this work since, in the operation conditions considered here, the air is relatively far from being water-saturated; and therefore it is logical that the obtained $\lambda_{\mathrm{H_2O/SO_3^-}}$ values are clearly lower than 14.

As in section 4.1, in this work only the fitting to the experimental data extracted from experiment $(-;-;+)$ is shown, for the sake of clarity. Similar fitting goodness was achieved for all the other operation conditions considered in the experimental design. Moreover, the fitted model parameters are consistent with their physical meaning, in all the cases. It was deduced that the proposed empirical model successfully explains the experimental evolution of the water content of the PEM membrane, with the operation current.

4.3. Qualitative analysis of the effect of the operation parameters on the water content curve

In this section the effect of each one of the operation parameters on the water content curve will be analysed qualitatively. In order to achieve this, the water content curves obtained experimentally will be superimposed by pairs. For the sake of clarity, only one of the two replicas of each experiment will be presented in the qualitative analysis.

4.3.1. Effect of the operation temperature

Figure 3 shows the effect of the operation temperature on the water content curve, for different humidities of the inlet gases. On the one hand, it can be observed that for given inlet humidities, the operation temperature has a negative effect on the water content of the membrane at open circuit ($I_{DC} = 0\ A$): an increase in the operation temperature leads to a drop in parameter $\lambda^0_{H_2O/SO_3^-}$. On the other hand, the operation temperature has a negative effect on the saturation water content: for given inlet humidities, an

increase in the operation temperature causes a decrease in parameter $\lambda^{\infty}_{H_2O/SO_3^-}$. Finally, it can be observed that the water content curve presents a sharper increase (i.e. the saturation value is reached for lower currents) when the operation temperature is increased. This observation is equivalent to say that the operation temperature has a positive effect on the current effect parameter: an increase in the operation temperature, for given inlet humidities, leads to an increase in parameter κ_λ.

4.3.2. Effect of the hydrogen humidification temperature

Figure 4 shows the effect of the hydrogen humidification temperature (i.e. the inlet hydrogen humidity) on the water content curve, for different operation temperatures and air humidities. On the one hand, it can be observed that the hydrogen humidity has a positive effect on the water content of the membrane at $I_{DC} = 0\ A$: an increase in the hydrogen humidity leads to an increase in parameter $\lambda^{0}_{H_2O/SO_3^-}$. On the other hand, no clear trend in the saturation water content can be observed with the hydrogen humidity. This suggests that hydrogen humidity may not have a significant effect on parameter $\lambda^{\infty}_{H_2O/SO_3^-}$. Finally, it can be observed that the water content curve presents a less pronounced increase (i.e. the saturation value is reached for higher currents) when the hydrogen humidity is increased. This observation is equivalent to say that the hydrogen humidity has a negative effect on the current effect parameter: an increase in the hydrogen humidity, for a given operation temperature and air humidity, leads to a drop in parameter κ_λ.

4.3.3. Effect of the air humidification temperature

Figure 5 shows the effect of the air humidification temperature (i.e. the inlet air humidity) on the water content curve, for different operation temperatures and hydrogen humidities. On the one hand, it can be observed that for a given operation temperature and hydrogen humidity, the operation temperature has a positive effect on the water content of the membrane at open circuit: an increase in the air humidity leads to an increase of parameter $\lambda^0_{H_2O/SO_3^-}$. On the other hand, the air humidity has as well a positive effect on the saturation water content: for a given operation temperature and hydrogen humidity, an increase in the air humidity causes an increase in parameter $\lambda^\infty_{H_2O/SO_3^-}$. Finally, the saturation water curve slope does not present any clear trend with the air humidity. This suggests that the air humidity may not have a significant effect on parameter κ_λ.

4.4. Statistical analysis

A statistical analysis was performed in order to confirm quantitatively the qualitative observations presented in section 4.3. After repeating the analysis described in section 4.2 for experiment $(-;-;+)$ to the other 17 experiments, the fitted values of the 3 model parameters ($\lambda^0_{H_2O/SO_3^-}$, $\lambda^\infty_{H_2O/SO_3^-}$, and κ_λ) were obtained for every combination of operation conditions considered in the experimental design. An ANOVA analysis was performed in order to determine which factors (operation temperature and inlet humidities) have a statistically significant effect on each model parameter. Subsequently, the response surface method was used in order to obtain a regression

model that relates each model parameter with the factors that have a significant effect on it. All the statistical analysis performed in this work, were done using a confidence level of 95%.

4.4.1. ANOVA analysis

The results of the ANOVA analysis for the different model parameters are presented in Tables 4 to 6. The ANOVA analysis of the results indicates that while parameter $\lambda^{0}_{H_2O/SO_3^-}$ depends significantly on all three input factors (operation temperature, and inlet humidities); parameter $\lambda^{\infty}_{H_2O/SO_3^-}$ only depends on the operation temperature and on the air humidity; and parameter κ_λ only depends significantly on the operation temperature and the hydrogen humidity.

Certain hypothesis must be met for an ANOVA analysis to be valid: independence, statistical significance, normality, and homoscedasticity [59]. The validation of these hypotheses is mandatory before accepting the results of any ANOVA analysis. Firstly, in this work, the independence of the observations was guaranteed by the selection of a randomized experimental design. Secondly, statistical significance is assured for a residual number of degrees of freedom higher than 4. As it can be seen in Tables 4, 5 and 6, this condition is fulfilled in the 3 presented ANOVA studies. Finally, the fulfillment of the normality and homoscedasticity hypothesis can be verified using the residues of the ANOVA. On the one hand, in this work, the normality hypothesis was verified using the unidimensional statistics of the ANOVA residues (asymmetry and curtosís coefficients, box and whiskers plot, and normal probability plot), the Shapiro-Wilk test,

and the Kolmogorov-Smirnov test. On the other hand, in this work, the homoscedasticity hypothesis was verified using the residues versus observed plot. The 4 hypothesis were successfully validated for the 3 ANOVA studies; however, for the sake of briefness and clarity, all these validations were not presented in this document.

4.4.2. Regression models

In this work, a first order linear model with interactions was considered for parameters $\lambda^{\infty}_{H_2O/SO_3^-}$ and κ_λ. In each case, only the factors and the interactions that have a statistically significant effect on the parameter, which were determined in the ANOVA studies presented in section 4.4.1., were included in the regression model. In addition, it was determined that factors T and H_{air} have a statistically significant second order effect on parameter $\lambda^{0}_{H_2O/SO_3^-}$. For this reason, these two quadratic effects were included in the $\lambda^{0}_{H_2O/SO_3^-}$ regression model, in addition to the main effects and the interaction that have a significant effect on $\lambda^{0}_{H_2O/SO_3^-}$. The surface responses considered for each model parameter are given by the following expressions:

$$\lambda^{0}_{H_2O/SO_3^-} = \lambda^{0}_{cte} + \lambda^{0}_{T} \cdot T + \lambda^{0}_{H_{H_2}} \cdot H_{H_2} + \lambda^{0}_{H_{air}} \cdot H_{air} + \lambda^{0}_{T \cdot H_{H_2}} \cdot T \cdot H_{H_2} + \lambda^{0}_{T \cdot H_{air}} \cdot T \cdot H_{air} + \lambda^{0}_{T^2} \cdot T^2 + \lambda^{0}_{H^2_{air}} \cdot H^2_{air} \quad (11)$$

$$\lambda^{\infty}_{H_2O/SO_3^-} = \lambda^{\infty}_{cte} + \lambda^{\infty}_{T} \cdot T + \lambda^{\infty}_{H_{air}} \cdot H_{air} + \lambda^{\infty}_{T \cdot H_{air}} \cdot T \cdot H_{air} \quad (12)$$

$$\kappa_\lambda = \kappa_{cte} + \kappa_T \cdot T + \kappa_{H_{H_2}} \cdot H_{H_2} \quad (13)$$

In the above expression, T denotes the operation temperature, and H_i stands for the absolute humidity of gas i. Tables 7 to 9 give the values of the coefficients of the fitted regression models. These tables present the fitted value and the uncertainty for a 95% confidence level, of each one of the different parameters considered in each regression model. As it can be observed in the mentioned tables, the 3 regression models have determination coefficients higher than 90%, which indicate that the 3 regression models are able to perfectly reproduce the experimental data.

4.4.3. Parameter $\lambda^0_{H_2O/SO_3^-}$

Figure 6 shows the contour plot of the regression model obtained for parameter $\lambda^0_{H_2O/SO_3^-}$. On the one hand, for a given level of humidity in the inlet gases, an increase in the temperature leads to a drop in $\lambda^0_{H_2O/SO_3^-}$. On the other hand, for a given temperature, an increase in the humidity of any of the inlet gases, causes an increase in $\lambda^0_{H_2O/SO_3^-}$. As it was defined in section 4.2, parameter $\lambda^0_{H_2O/SO_3^-}$ is the open circuit effective water content of the membrane. In other words, $\lambda^0_{H_2O/SO_3^-}$ corresponds with the water content of the membrane when no current is circulating within the PEMFC. In open circuit, no water is produced in the cathodic compartment. Consequently, the open circuit water content of the membrane is determined by 2 processes. The first one is the water absorption from the inlet humidified gases. The second one is the water loss due to the water drag by the gas streams that flow through the PEMFC. For given operation conditions (temperature and inlet humidities), a balance between both

processes is reached. The water content of the membrane in the aforementioned equilibrium corresponds with $\lambda^0_{H_2O/SO_3^-}$ for those operation conditions.

For given humidity levels in the inlet gases, an increase in the operation temperature causes an increase in the water vapor pressure on the PEM membrane, which in turn causes an increase of the water losses by drag. Since the intake term remains unmodified, the increase of the loss term causes a shift of the equilibrium point toward lower membrane water contents. This explains why an increase of T, for given H_{H_2} and H_{air}, results in a drop in $\lambda^0_{H_2O/SO_3^-}$. On the contrary, an increase of the humidity of either of the 2 inlet gases, for a given temperature, results in an increase of the water intake term, which shifts the equilibrium point toward higher membrane water contents. This explains why, for a given T, an increase in H_{H_2} or H_{air} causes an increase in $\lambda^0_{H_2O/SO_3^-}$. Finally, because of the gas flow rates used in this work, the absolute amount of water introduced by the air stream is substantially greater than the water amount carried by the hydrogen stream. This is the reason why the magnitude of the effect of factor H_{air} on $\lambda^0_{H_2O/SO_3^-}$ is significantly higher than the magnitude of the effect of factor H_{H_2}.

4.4.4. Parameter $\lambda^\infty_{H_2O/SO_3^-}$

Figure 7 shows the contour plot of the regression model obtained for parameter $\lambda^\infty_{H_2O/SO_3^-}$. On the one hand, for a given level of air humidity, an increase in the operation temperature leads to a drop of $\lambda^\infty_{H_2O/SO_3^-}$. On the other hand, for a given temperature, an increase of the air humidity causes an increase of $\lambda^\infty_{H_2O/SO_3^-}$. As it was defined in

section 4.2, parameter $\lambda^{\infty}_{H_2O/SO_3^-}$ is the saturation effective water content of the membrane. In other words, $\lambda^{\infty}_{H_2O/SO_3^-}$ corresponds with the water content of the membrane when a high current is circulating through the PEMFC. In such situation, the water production in the cathodic compartment is significant. As parameter $\lambda^{0}_{H_2O/SO_3^-}$, parameter $\lambda^{\infty}_{H_2O/SO_3^-}$ is also determined by a balance between the process of water absorption from the inlet humidified gases, and the process of water loss by water drag by the gas flows. However, in the case of parameter $\lambda^{\infty}_{H_2O/SO_3^-}$, there is a third process that affects significantly the equilibrium: the water production due to the cathodic half-reaction.

The trends of $\lambda^{\infty}_{H_2O/SO_3^-}$ with the operation temperature and the inlet humidities are due to the same reasons that explain the trends observed in parameter $\lambda^{0}_{H_2O/SO_3^-}$. On the one hand, for a given air humidity, an increase in the temperature causes an increase in the water loss term, which results in a shift of the equilibrium towards lower water content values. This explains why an increase in T, for a given H_{air}, results in a drop in $\lambda^{\infty}_{H_2O/SO_3^-}$. On the other hand, an increase in the air humidity, for a given temperature, causes an increase in the membrane water intake, which results in the displacement of the equilibrium towards higher water content values. This is the reason why an increase in H_{air}, for a given T, results in an increase of $\lambda^{\infty}_{H_2O/SO_3^-}$.

When comparing Figures 6 and 7, it can be observed that $\lambda^{\infty}_{H_2O/SO_3^-}$ is higher than $\lambda^{0}_{H_2O/SO_3^-}$ in every point of the phase space. At given operation conditions (temperature and inlet humdities), the water production process shifts the equilibrium toward higher

water content values, with respect to the open circuit case in which this third process is absent. This explains why $\lambda^{\infty}_{H_2O/SO_3^-}$ is greater than $\lambda^{0}_{H_2O/SO_3^-}$ for any given operation conditions.

Unlike parameter $\lambda^{0}_{H_2O/SO_3^-}$, parameter $\lambda^{\infty}_{H_2O/SO_3^-}$ is not significantly affected by hydrogen humidity. This is because the absolute amount of water carried by the hydrogen stream is small, due to the selected hydrogen flow rate. In conditions where the amount of water produced in the cathodic compartment is high (i.e. high current intensities), the amount of water introduced by the hydrogen stream is negligible with respect to the produced water amount. In contrast, in conditions where the amount of water produced in the cathode is small (i.e. open circuit), even the small contribution of water by the hydrogen stream has a significant effect. This explains why H_{H_2} has a significant effect on $\lambda^{0}_{H_2O/SO_3^-}$, whereas it has no significant effect on $\lambda^{\infty}_{H_2O/SO_3^-}$.

4.4.5. Parameter κ_λ

Figure 8 shows the contour plot of the regression model obtained for parameter κ_λ. On the one hand, for a given level of hydrogen humidity, an increase in the operation temperature leads to an increase of κ_λ. On the other hand, for a given temperature, an increase of the hydrogen humidity causes a drop of κ_λ. As it was defined in section 4.2, parameter κ_λ is the parameter that quantifies the magnitude of the effect of I_{DC} on λ_{H_2O/SO_3^-}. In other words, a high value of κ_λ means that small changes in the operation current cause big changes in the water content of the PEM membrane; and on the contrary, a low value of κ_λ means that big changes in the polarization current leads to

small changes in the membrane water content. Since water is produced in the cathodic compartment, the concentration of water on the surface of the PEM membrane in contact with the cathodic compartment is significantly higher than the water concentration on the surface of the PEM membrane in contact with the anodic compartment. This water concentration gradient generates a flow of water from the cathodic compartment to the anodic compartment. This water flux is one of the contributors to the hydration of the internal regions of the PEM membrane.

On the one hand, an increase in the operation temperature results in an increase of water diffusivity in Nafion® [73], and therefore, in an increase on the water diffusivity in the PEM membrane. For this reason, at higher temperatures, a given change in the water production in the cathode (i.e. a given change in I_{DC}), results in a bigger change in the water flux through the membrane, and therefore, in a higher change in the membrane's water content. This is the reason why, as the operation temperature increases, the operation current has a greater effect on the water content of the membrane. In other words, this explains why κ_λ increases with T. On the other hand, an increase in the hydrogen humidity results in an increase of the water concentration in the anodic compartment, in general; and on the surface of the PEM membrane in contact with the anodic compartment, in particular. This results in a drop in the driving force of the water flux from the cathodic to the anodic compartment. Thus, for a given change in the water production in the cathode (i.e. a given change in I_{DC}), the water flux through the membrane is smaller; and consequently, the membrane's water content change is also smaller. This explains why the operation current effect on the water

content of the membrane decreases when hydrogen humidity increases; which is equivalent to say that κ_λ decreases with H_{H_2}.

5. Conclusions

The proposed semiempirical model successfully achieves to describe the experimental behaviour of the internal resistance of the PEMFC with the DC current. The main advantage of the proposed semiempirical model is that even if it is an empirical model (thus, easy to use); all the parameters of the proposed model have a defined physical interpretation.

The performed statistical analysis allowed to determine which operation parameters (operation temperature and inlet humidities) have a statistically significant effect on each one of the three parameters of the semiempirical model of the effect of operation current on the internal resistance of a PEM fuel cell. On the one hand, all three operation parameters have a significant effect on the open circuit water content parameter. On the other hand, only the operation temperature and the air humidity have a significant effect on the saturation parameter. Finally, only the operation temperature and the hydrogen humidity have a significant effect on the characteristic current parameter.

6. Nomenclature

Latin letters

$\mathrm{A_{PEM}}$	Active area of the PEM membrane (m^2)
H_i	Absolute humidity of stream i $\left(g_{H_2O} \cdot g_{dry\ gas}^{-1}\right)$
I	Current (A)
I_{DC}	Operation current (A)
$\mathrm{l_{PEM}}$	Thickness of the PEM membrane (m)
R^2	Determination coefficient $(\%)$
R_{cont}	Contact resistance (Ω)
R_{int}	Internal resistance (Ω)
R_{int}^{ele}	Electronic resistance (Ω)
R_{int}^{ion}	Ionic resistance (Ω)
$\mathrm{r_{PEM}}$	Ionic resistivity of the PEM membrane $(\Omega \cdot \mathrm{m})$
T	Operation temperature (K)
$\mathrm{T_{H_2}^{hum}}$	Hydrogen humidification temperature (K)
$\mathrm{T_{air}^{hum}}$	Air humidification temperature (K)

Greek letters

η_{Ohmic}	Ohmic overvoltage (V)
κ_λ	Current effect parameter (A^{-1})
$\lambda_{\mathrm{H_2O/SO_3^-}}$	Effective water content of the membrane

$\lambda^{0}_{H_2O/SO_3^-}$	Open circuit effective water content of the membrane
$\lambda^{\infty}_{H_2O/SO_3^-}$	Saturation effective water content of the membrane

Subscripts

cte	Constant term
H_{air}	Air humidity main effect term
H^2_{air}	Air humidity quadratic effect term
H_{H_2}	Hydrogen humidity main effect term
T	Temperature main effect term
T^2	Temperature quadratic effect term
$T \cdot H_{air}$	Temperature-air humidity interaction term
$T \cdot H_{H_2}$	Temperature-hydrogen humidity interaction term

7. Acknowledgments

The authors are very grateful to the Generalitat Valenciana for its economic support in form of Vali+d grant (Ref: ACIF-2013-268).

8. Bibliography

[1] R. Maizia, A. Dib, A. Thomas, S. Martemianov, J. Power Sources 342 (2017) 553-561.

[2] W.K. Epting, S. Litster, J. Power Sources 306 (2016) 674-684.

[3] J.J. Giner-Sanz, E.M. Ortega, V. Pérez-Herranz, Fuel Cells 15 (2015) 479-493.

[4] H. Fathi, A. Raoof, S.H. Mansouri, J. Power Sources 349 (2017) 57-67.

[5] J.J. Giner-Sanz, E.M. Ortega, V. Pérez-Herranz, Int. J. Hydrogen Energy, 39 (2014) 13206-13216.

[6] M. Tanaka, Y. Takeda, T. Wakiya, Y. Wakamoto, K. Harigaya, T. Ito, T. Tarao, H. Kawakami, J. Power Sources 342 (2017) 125-134.

[7] E.J. Oh, R. Hempelmann, V. Nica, I. Radev, H. Natter, J. Power Sources 341 (2017) 240-249.

[8] Y. Singh, F.P. Orfino, M. Dutta, E. Kjeang, J. Power Sources 345 (2017) 1-11.

[9] M. Wei, M. Jiang, X. Liu, M. Wang, S. Mu, J. Power Sources 327 (2016) 384-393.

[10] Y. Wang, L. Yue, S. Wang, J. Power Sources 344 (2017) 32-38.

[11] H. Ito, Y. Heo, M. Ishida, A. Nakano, S. Someya, T. Munakata, J. Power Sources 342 (2017) 393-404.

[12] A. Ebadighajari, J. DeVaal, F. Golnaraghi, J. Power Sources 340 (2017) 247-257.

[13] H. Han, H.Q. Li, M. Liu, L. Xu, J. Xu, S. Wang, H. Ni, Z. Wang, J. Power Sources 340 (2017) 126-138.

[14] T. Söndergaard, L.N. Cleemann, H. Becker, D. Aili, T. Steenberg, H.A. Hjuler, L. Seerup, Q. Li, J.O. Jensen, J. Power Sources, 342 (2017) 570-578.

[15] S. Abbou, J. Dillet, G. Maranzana, S. Didierjean, O. Lottin, J. Power Sources 340 (2017) 419-427.

[16] Z. Zhu, X. Yan, H. Tang, H. Cai, M. Pan, H. Zhang, J. Luo, J. Power Sources 351 (2017) 138-144.

[17] M.G. Poulsen, M.J. Larsen, S.M. Andersen, J. Power Sources 343 (2017) 174-182.

[18] C. Robin, M. Gerard, M. Quinaud, J. d'Arbigny, Y. Bultel, J. Power Sources 326 (2016) 417-427.

[19] E. Ozden, I. Tari, J. Power Sources 304 (2016) 64-73.

[20] X. Wan, H. Wang, H. Yu, F. Peng, J. Power Sources 346 (2017) 80-88.

[21] B. Zhang, J. Ni, X. Xiang, L. Wang, Y. Chen, J. Power Sources 337 (2017) 110-117.

[22] M. Renzi, G. D'Angelo, R. Marassi, F. Nobili, J. Power Sources 327 (2016) 11-20.

[23] D. Ebenezer, A.P. Deshpande, P. Haridoss, J. Power Sources 304 (2016) 282-292.

[24] F.N. Büchi, G.G. Scherer, J. Electroanal. Chem. 404 (1996) 37-43.

[25] F. Barbir, PEM fuel cells: theory and practice. Academic Press, London, 2013.

[26] S. Renganathan, Q. Guo, V.A. Sethuraman, J.W. Weidner, R.E. White, J. Power Sources 160 (2006) 386-397.

[27] H.L. Yeager, A. Steck, J. Electrochem. Soc. 128 (1981) 1880-1884.

[28] W.Y. Hsu, T.D. Gierke, J. Mem. Sci. 13 (1983) 307-326.

[29] M. Eikerling, A.A. Kornyshev, U. Stimming, J. Phys. Chem. B 101 (1997) 10807-10820.

[30] S.J. Paddison, R. Paul, T.A. Zawodzinski, J. Electrochem. Soc. 147 (2000) 617-626.

[31] Y. Yang, P.N. Pintauro, AIChE J. 46 (2000) 1177- 1190.

[32] P. Cormmer, A.G. Cherstvy, E. Spohr, A.A. Kornyshev, Fuel Cells 2 (2002) 127- 136.

[33] J. Fimrite, B. Carnes, H. Struchtrup, N. Djilali, J. Electrochem. Soc. 152 (2005) A1815-A1823.

[34] P. Choi, N.H. Jalani, R. Datta, J. Electrochem. Soc. 152 (2005) E123- E130.

[35] M. Ceraolo, C. Miulli, A. Pozio, J. Power Sources 113 (2003) 131-144.

[36] H.I Kim, C.Y. Cho, J.H. Nam, S. Donghoon, T.Y. Chung, Int. J. Hydrogen. Energ. 35 (2010) 3656-3663.

[37] P.R. Pathapati, X. Xue, J. Tang, Renew. Energ. 30 (2005) 1-22.

[38] C. Wang, M.H. Nehrir, S.R. Shaw, IEEE T. Energy Conver. 20 (2005) 442-451.

[39] M.V. Moreira, G.E. Da Silva, Renew. Energ. 34 (2009) 1734-1741.

[40] C. Ziogou, S. Voutetakis, S. Papadopoulou, M.C. Georgiadis, Comput. Chem. Eng. 35 (2011) 1886-1900.

[41] A. Saadi, M. Becherif, D. Hissel, H.S. Ramadan, Int. J. Hydrogen. Energ. 42 (2017) 1544-1557.

[42] J.C. Amphlett, R.M. Baumert, R.F. Mann, B.A. Peppley, P.R. Roberge, T.J. Harris, J. Electrochem. Soc. 142 (1995) 1-8.

[43.] J.C. Amphlett, R.M. Baumert, R.F. Mann, B.A. Peppley, P.R. Roberge, J. Electrochem. Soc. 142 (1995) 9-15.

[44] T.E. Springer, T.A. Zawodzinski, S. Gottesfeld, J. Electrochem. Soc. 138 (1991) 2334-2342.

[45] J.T. Wang, R.F. Savinell, Electrochim. Acta 37 (1992) 2737- 2745.

[46] T.V. Nguyen, R.E. White, J. Electrochem. Soc. 140 (1993) 2178-2186.

[47] D.M. Bernardi, M.W. Verbrugge, J. Electrochem. Soc. 139 (1992) 2477-2491.

[48] G. Murgia, L. Pisani, M. Valentini, B. D'Aguanno, J. Electrochem. Soc. 149 (2002) A31- A38.

[49] M. Eikerling, Y.I. Kharkats, A.A. Kornyshev, Y.M. Volfkovich, J. Electrochem. Soc. 145 (1998) 2684- 2699.

[50] K. Ou, W.W. Yuan, M. Choi, S. Yang, Y.B. Kim, Int. J. Hydrogen. Energ. 42 (2017) 29852-29862.

[51] S.K. Park, S.Y. Choe, J. Power Sources 179 (2008) 660-672.

[52] S.M. Sharifi-Asl, S. Rowshanzamir, M.H. Eikani, Energy 35 (2010) 1633-1646.

[53] A. Vasilyev, J. Andrews, L.M. Jackson, S.J. Dunnett, B. Davies, Int. J. Hydrogen. Energ. 42 (2017) 29406-29421.

[54] J.D.A. Larminie, Fuel cell system explained, 2nd ed., John Wiley & Sons, New York, 2003.

[55] T. Thampan, S. Malhortra, H. Tang, R. Datta, J. Electrochem. Soc. 147 (2000) 3242-3250

[56] G.J.M. Janssen, J. Electrochem. Soc. 148 (2001) A1313- A1323.

[57] W. Friede, S. Raël, B. Davat, IEEE T. Power Electr. 19 (2004) 1234-1241.

[58] A.Z. Weber, J. Newman, J. Electrochem. Soc. 151 (2004) A311-A325.

[59] D.C. Montgomery, Design and analysis of experiments, John Wiley & Sons, Hoboken, 2008.

[60] J.J. Giner-Sanz, E.M. Ortega, V. Pérez-Herranz, Fuel Cells 16 (2016) 469–479.

[61] J.J. Giner-Sanz, E.M. Ortega, V. Pérez-Herranz, Electrochim. Acta 174 (2015) 1290-1298.

[62] M.E. Orazem, B. Tribollet, Electrochemical Impedance Spectroscopy, John Wiley & Sons, Hoboken, 2008.

[63] J.J. Giner-Sanz, E.M. Ortega, V. Pérez-Herranz, Fuel Cells 17 (2017) 391-401.

[64] J.J. Giner-Sanz, E.M. Ortega, V. Pérez-Herranz, Electrochim. Acta 186 (2015) 598-612.

[65] J.J. Giner-Sanz, E.M. Ortega, V. Pérez-Herranz, Electrochim. Acta 211 (2016) 1076-1091.

[66] J.J. Giner-Sanz, E.M. Ortega, V. Pérez-Herranz, J. Electrochem. Soc. 164 (2017) H918-H924.

[67] J.J. Giner-Sanz, E.M. Ortega, V. Pérez-Herranz, Int. J. Hydrogen Energy 40 (2015) 11279-11293.

[68] J.J. Giner-Sanz, E.M. Ortega, V. Pérez-Herranz, Electrochim. Acta 209 (2016) 254-268.

[69] X.Z.R. Yuan, Electrochemical impedance spectroscopy in PEM fuel cells: fundamentals and applications, Springer Science & Business Media, London, 2009.

[70] F. Chen, Y. Gao, Fuel Cells 15 (2015) 337-343.

[71] R.F. Mann, J.C. Amphlett, M.A. Hooper, H.M. Jensen, B.A. Peppley, P.R. Roberge, J. Power Sources 86 (2000) 173-180.

[72] G. Hu, J. Fan, J. Power Sources 165 (2007) 171-184.

[73] T.A. Zawodzinski, C. Derouin, S. Radzinski, R.J. Sherman, V.T. Smith, T.E. Springer, S. Gottesfeld, J. Electrochem. Soc. 140 (1993) 1041-1047.

Table 1. Quantitative values of the encoded factor levels

Factor	Level -1	Level 0	Level +1
Temperature (℃)	30	50	70
Hydrogen humidity ($g_{H_2O} \cdot g^{-1}_{dry\ H_2}$)	0.28	1.26	2.25
Air humidity ($mg_{H_2O} \cdot g^{-1}_{dry\ air}$)	3.5	9.8	16.0

Table 2. EIS measurement parameters

Measurement parameter	Value
Integration time	$1.0\ s$
Number of integration cycles	$5\ cycles$
Number of stabilization cycles	$15\ cycles$
Maximum stabilization time	$1.0\ s$
Minimum stabilization cycle fraction	0.00

Table 3. Fitted model parameters obtained from fitting the experimental $\boldsymbol{\lambda}$ vs $\boldsymbol{I_{DC}}$ curve, obtained in experiment $(-;-;+)$

Parameter	Units	Fitted value	Uncertainty (95% CL)
$\lambda^0_{H_2O/SO_3^-}$	-	7.936	± 0.057
$\lambda^\infty_{H_2O/SO_3^-}$	-	9.404	± 0.084
κ_λ	A^{-1}	0.276	± 0.040
R^2	%	98.57	

Table 4. ANOVA table for parameter $\boldsymbol{\lambda^0_{H_2O/SO_3^-}}$

Factor	Sum of squares	Degrees of freedom	Mean square	F ratio	p-value
Main effects					
T	66.6	1	66.6	947.87	0.0000
H_{H_2}	1.21	1	1.21	17.27	0.0016
H_{air}	17.2	1	17.2	244.76	0.0000
Interactions					
$T \cdot H_{H_2}$	1.11	1	1.11	15.75	0.0022
$T \cdot H_{air}$	11.3	1	11.3	161.39	0.0000
$H_{H_2} \cdot H_{air}$	6.36×10^{-3}	1	6.36×10^{-3}	0.09	0.7692
Residual	0.632	9	0.0702		
Total	98.1	15			

Table 5. ANOVA table for parameter $\boldsymbol{\lambda^\infty_{H_2O/SO_3^-}}$

Factor	Sum of squares	Degrees of freedom	Mean square	F ratio	p-value
Main effects					
T	46.1	1	46.1	173.33	0.0000
H_{H_2}	0.997	1	0.997	3.75	0.0849
H_{air}	7.15	1	7.15	26.86	0.0006
Interactions					
$T \cdot H_{H_2}$	0.531	1	0.531	1.99	0.1915
$T \cdot H_{air}$	1.99	1	1.99	7.50	0.0229
$H_{H_2} \cdot H_{air}$	0.226	1	0.226	0.85	0.3811
Residual	1.60	6	0.226		
Total	58.6	12			

Table 6. ANOVA table for parameter $\boldsymbol{\kappa_\lambda}$

Factor	Sum of squares	Degrees of freedom	Mean square	F ratio	p-value
Main effects					
T	0.0470	1	0.0470	10.33	0.0106
H_{H_2}	0.0342	1	0.0342	7.53	0.0227
H_{air}	9.22×10^{-6}	1	9.22×10^{-6}	0.00	0.9651
Interactions					
$T \cdot H_{H_2}$	8.22×10^{-3}	1	8.22×10^{-3}	1.81	0.2117
$T \cdot H_{air}$	3.29×10^{-3}	1	3.29×10^{-3}	0.72	0.4169
$H_{H_2} \cdot H_{air}$	7.15×10^{-3}	1	7.15×10^{-3}	1.57	0.2414
Residual	0.0409	9	4.55×10^{-3}		
Total	0.141	15			

Table 7. Coefficients of the regression model of parameter $\boldsymbol{\lambda^0_{H_2O/SO_3^-}}$

Parameter	Units	Fitted value	Uncertainty (95% CL)
λ^0_{cte}	-	9.856	± 0.036
λ^0_T	$°C^{-1}$	-0.0301	± 0.0027
$\lambda^0_{H_{H_2}}$	$g_{H_2} \cdot g^{-1}_{H_2O}$	-0.371	± 0.066
$\lambda^0_{H_{air}}$	$g_{air} \cdot g^{-1}_{H_2O}$	-167.34	± 0.85
$\lambda^0_{T \cdot H_{H_2}}$	$g_{H_2} \cdot g^{-1}_{H_2O} \cdot °C^{-1}$	0.0131	± 0.0043
$\lambda^0_{T \cdot H_{air}}$	$g_{air} \cdot g^{-1}_{H_2O} \cdot °C^{-1}$	6.66	± 0.10
$\lambda^0_{T^2}$	$°C^{-2}$	-0.00153	± 0.00052
$\lambda^0_{H^2_{air}}$	$g^2_{air} \cdot g^{-2}_{H_2O}$	-3.15	± 0.12
R^2	%	99.87	

Table 8. Coefficients of the regression model of parameter $\boldsymbol{\lambda^{\infty}_{H_2O/SO_3^-}}$

Parameter	Units	Fitted value	Uncertainty (95% CL)
λ^{∞}_{cte}	-	12.83	± 0.72
λ^{∞}_{T}	$°C^{-1}$	-0.131	± 0.015
$\lambda^{\infty}_{H_{air}}$	$g_{air} \cdot g^{-1}_{H_2O}$	-2.92	± 0.60
$\lambda^{\infty}_{T \cdot H_{air}}$	$g_{air} \cdot g^{-1}_{H_2O} \cdot °C^{-1}$	2.42	± 0.12
R^2	%	94.64	

Table 9. Coefficients of the regression model of parameter $\boldsymbol{\kappa_{\lambda}}$

Parameter	Units	Fitted value	Uncertainty (95% CL)
κ_{cte}	A^{-1}	0.223	± 0.045
κ_{T}	$A^{-1} \cdot °C^{-1}$	0.00279	± 0.00077
$\kappa_{H_{H_2}}$	$A^{-1} \cdot g_{air} \cdot g^{-1}_{H_2O}$	-0.0719	± 0.0016
R^2	%	90.59	

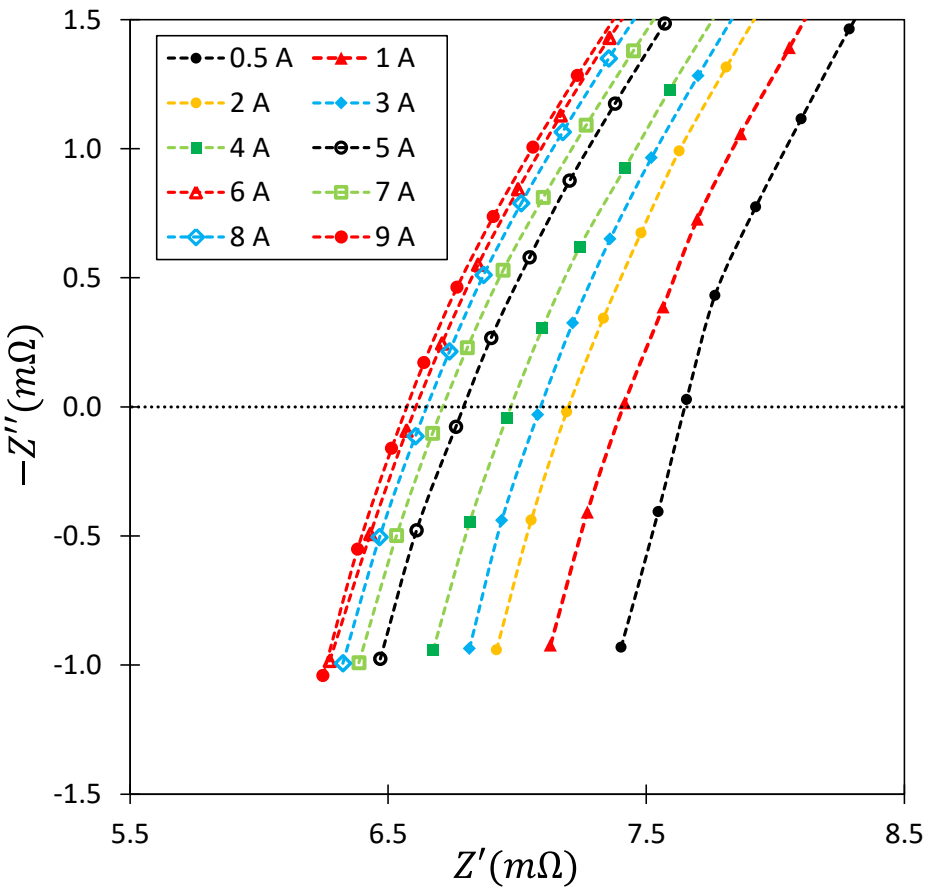

Figure 1. High frequency intercept with the real axis of the experimental spectra obtained for different operation currents, for experiment $(-;-;+)$

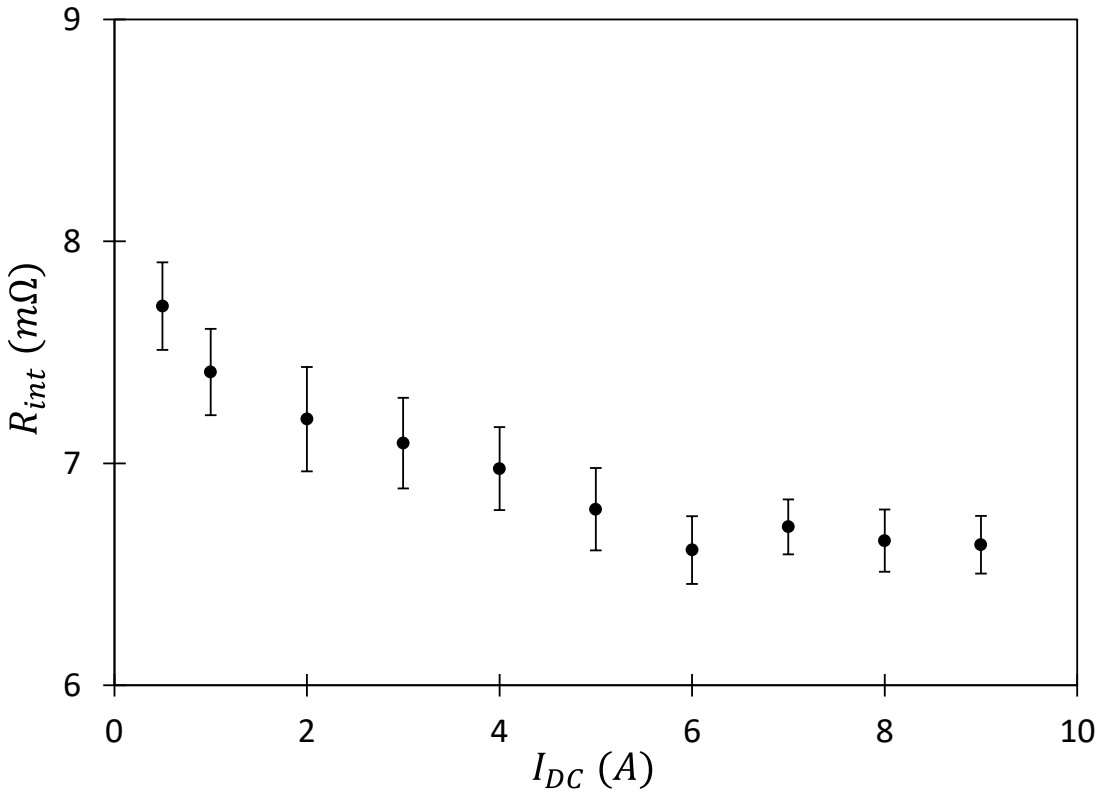

(a) R_{int}

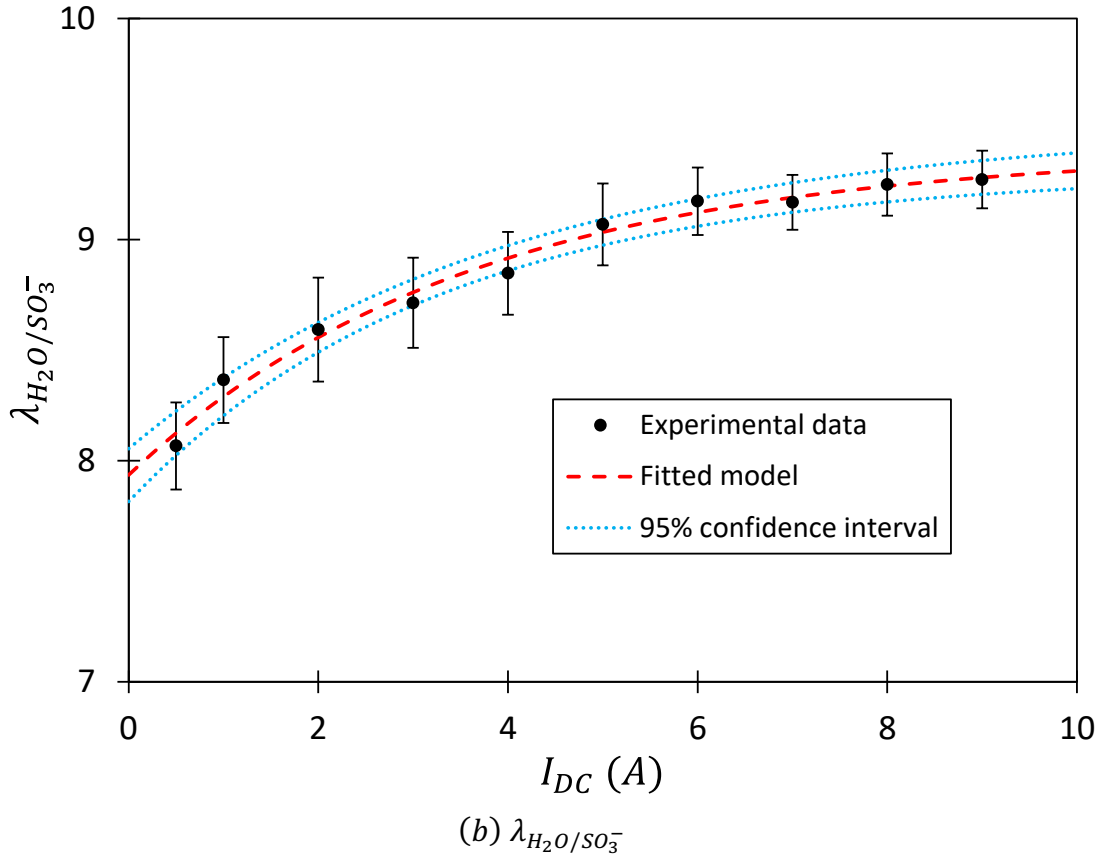

(b) λ_{H_2O/SO_3^-}

Figure 2. Evolution of the internal resistance and the water content of the membrane, with the operation current, for experiment $(-;-;+)$

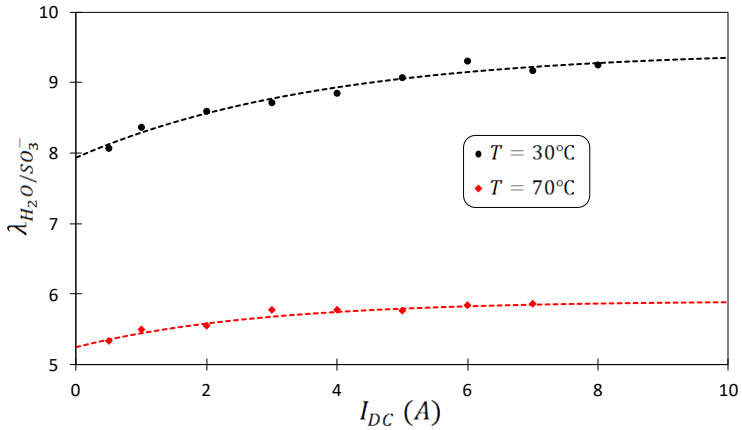

(a) $\mathrm{T}_{\mathrm{H_2}}^{\mathrm{hum}} = 30°\mathrm{C};\ \mathrm{T}_{\mathrm{air}}^{\mathrm{hum}} = 70°\mathrm{C}$

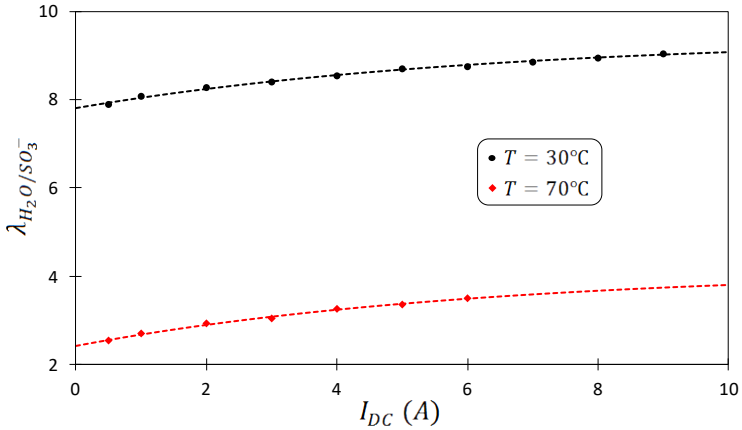

(b) $\mathrm{T}_{\mathrm{H_2}}^{\mathrm{hum}} = 70°\mathrm{C};\ \mathrm{T}_{\mathrm{air}}^{\mathrm{hum}} = 30°\mathrm{C}$

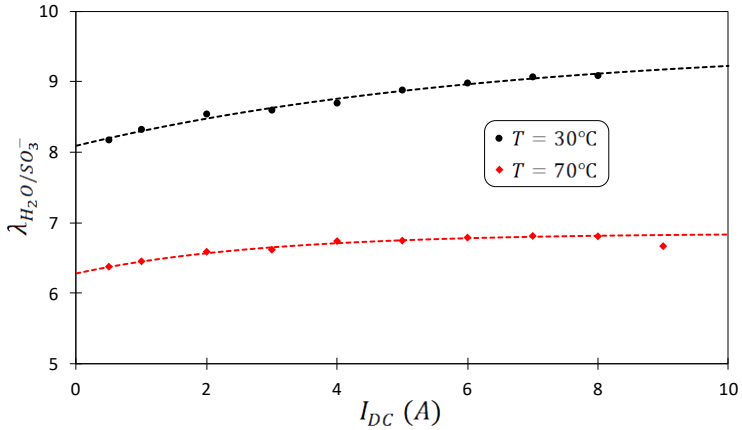

(c) $\mathrm{T}_{\mathrm{H_2}}^{\mathrm{hum}} = 70°\mathrm{C};\ \mathrm{T}_{\mathrm{air}}^{\mathrm{hum}} = 70°\mathrm{C}$

Figure 3. Effect of the operation temperature on the water content curve

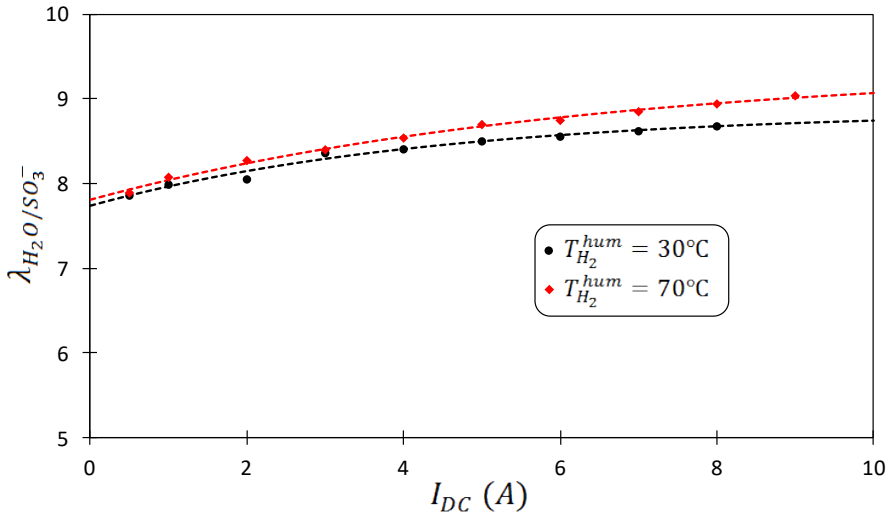

(a) T = 30°C; T_{air}^{hum} = 30°C

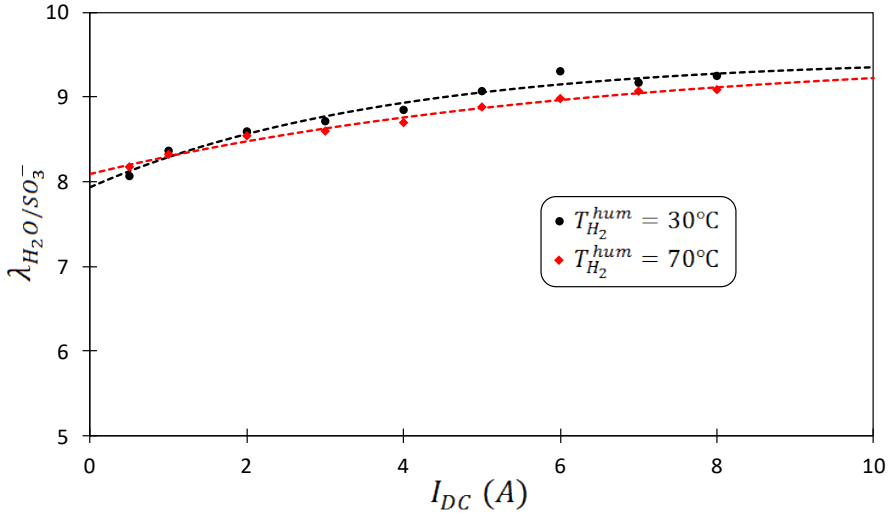

(b) T = 30°C; T_{air}^{hum} = 70°C

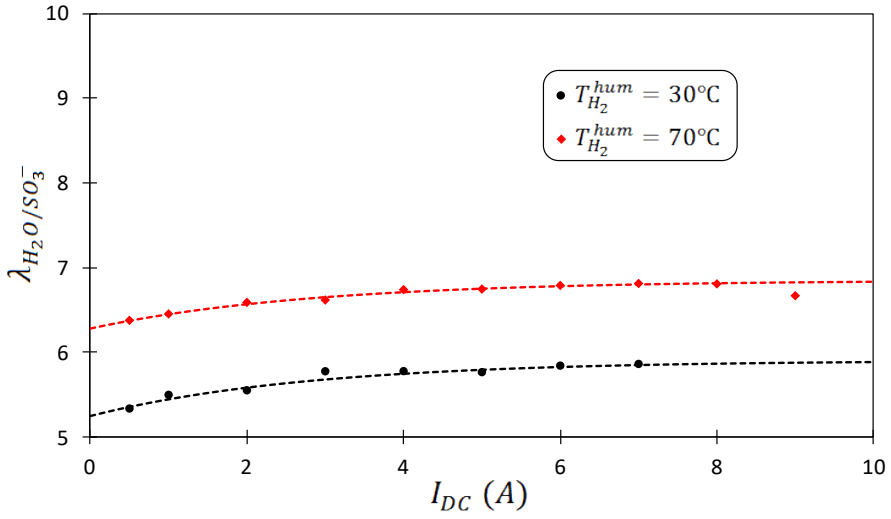

(c) T = 70°C; T_{air}^{hum} = 70°C

Figure 4. Effect of the hydrogen humidification temperature on the water content curve

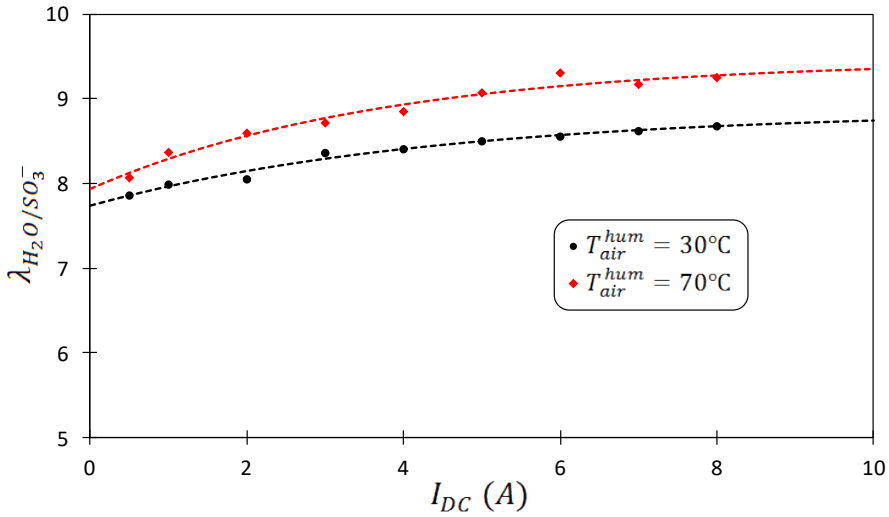

(a) T = 30°C; $T_{H_2}^{hum}$ = 30°C

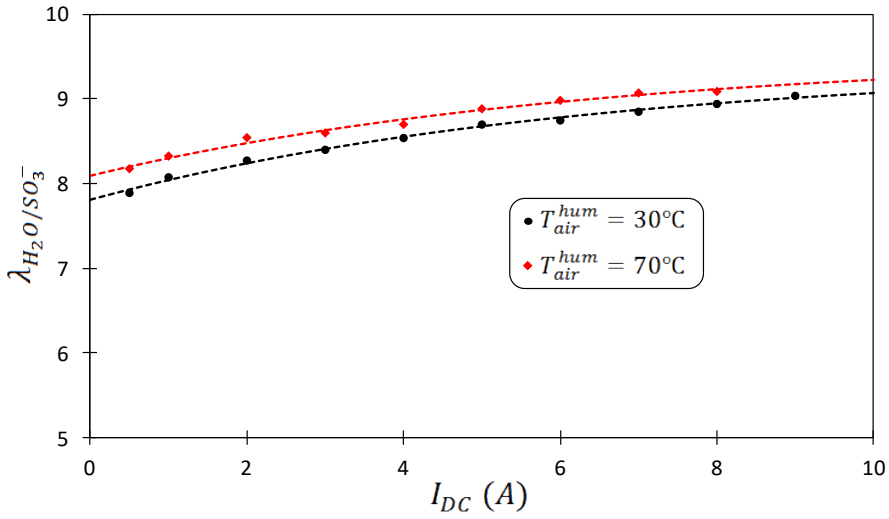

(b) T = 30°C; $T_{H_2}^{hum}$ = 70°C

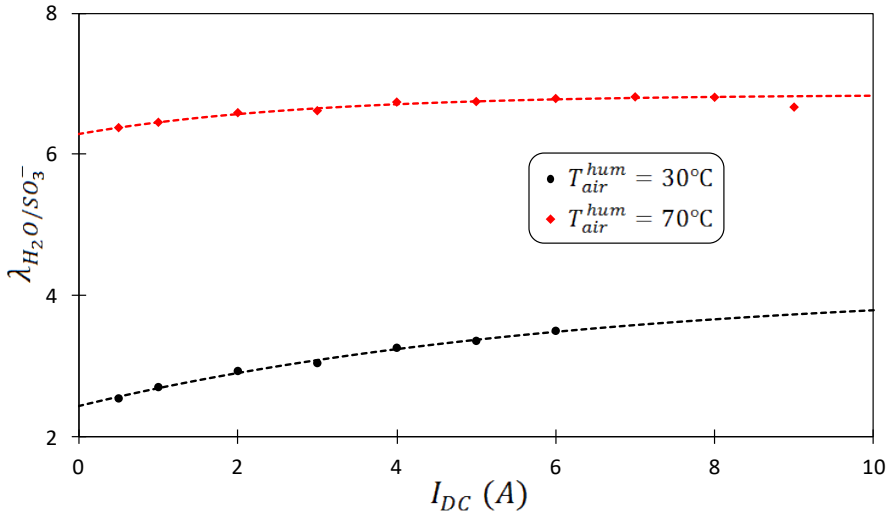

(c) T = 70°C; $T_{H_2}^{hum}$ = 70°C

Figure 5. Effect of the air humidification temperature on the water content curve

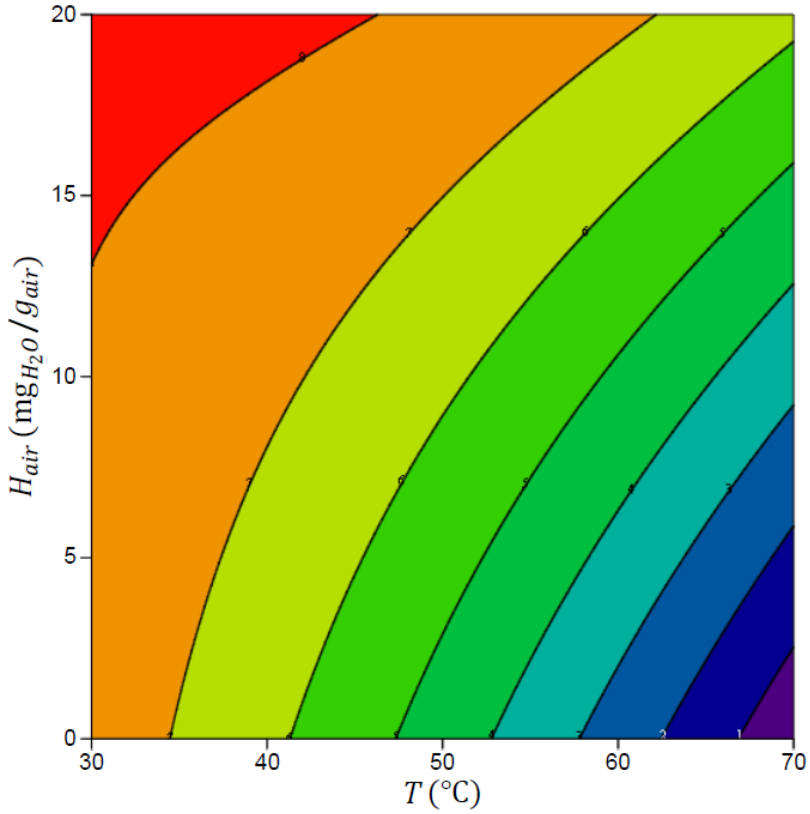

$(a)\ H_{H_2} = 0.000\ g_{H_2O} \cdot g_{H_2}^{-1}$

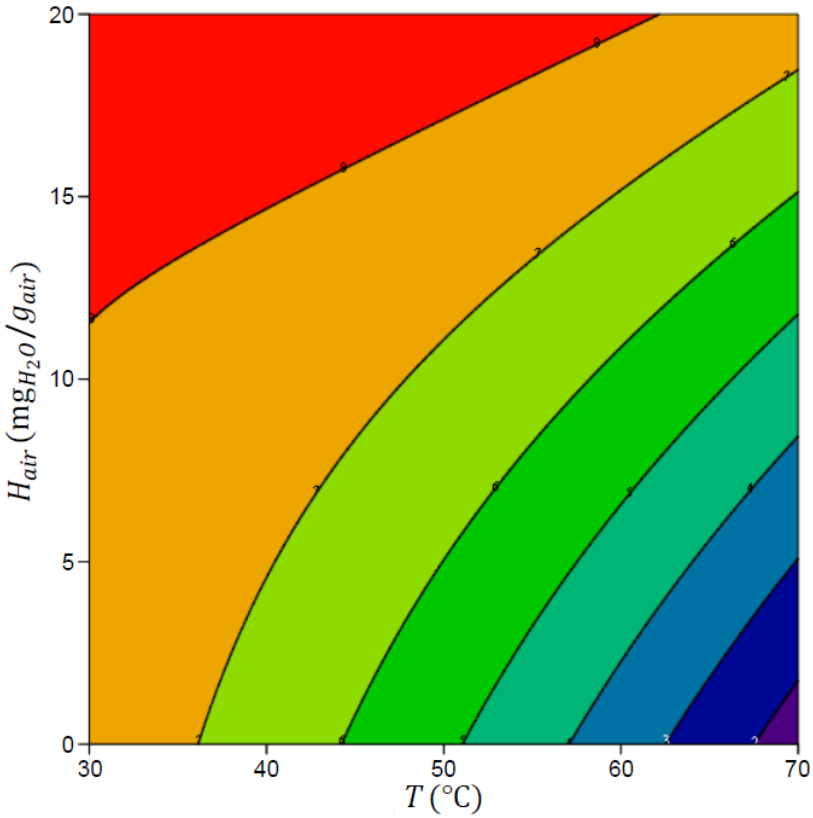

$(b)\ H_{H_2} = 2.247\ g_{H_2O} \cdot g_{H_2}^{-1}$

Figure 6. Contour plot of the regression model obtained for parameter $\boldsymbol{\lambda^0_{H_2O/SO_3^-}}$

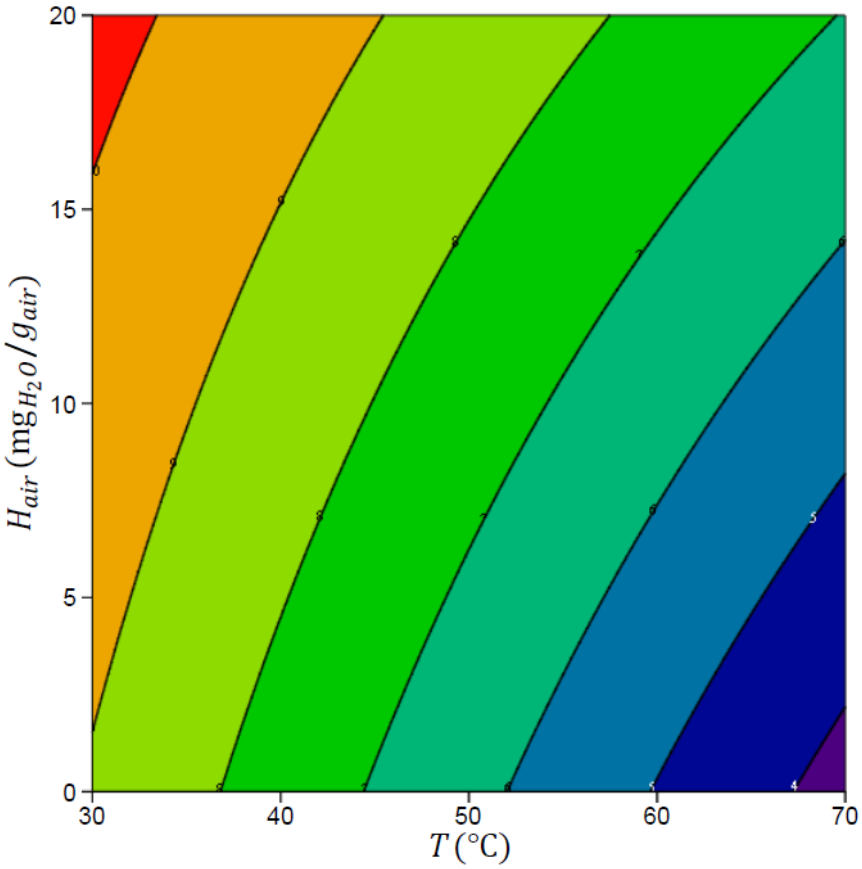

Figure 7. Contour plot of the regression model obtained for parameter $\boldsymbol{\lambda^{\infty}_{H_2O/SO_3^-}}$

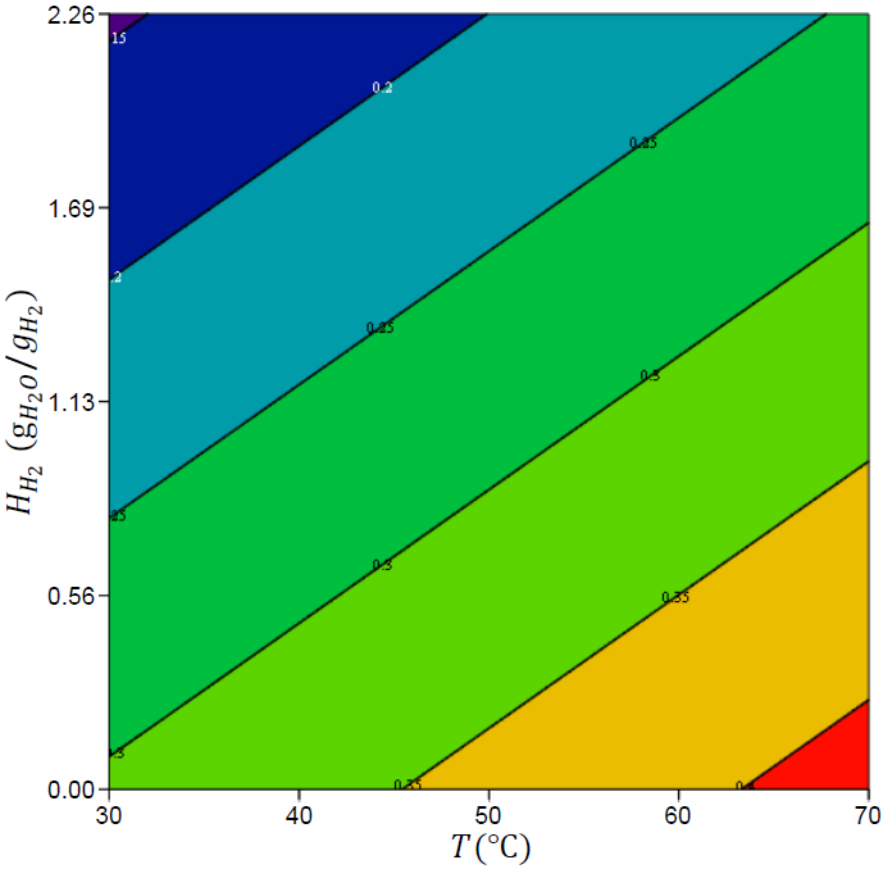

Figure 8. Contour plot of the regression model obtained for parameter κ_λ, expressed in A^{-1}